

Surface Polishing for Additively Manufactured Titanium Bone Scaffolds to Improve Osseointegration

Runrun Chen¹, Axel Fernandes¹, Changyu Ma¹, Shuyi Huang¹, Shiqi Zheng², Natan Barros³, Nhut Ho¹,
Bingbing Li^{1,4}

¹Autonomy Research Center for STEAHM (ARCS), California State University, Northridge, CA 91324

²Department of Material Science and Engineering, University of California Los Angeles, Los Angeles,
CA 90095

³Terasaki Institute for Biomedical Innovation, Los Angeles, CA 90024

⁴Department of Manufacturing Systems Engineering and Management, California State University,
Northridge, CA 91330

Abstract

This research focuses on the porous design, metal additive manufacture and surface polishing methods of Ti6Al4V alloy scaffolds for bone implants and tissue regeneration, with varying lattice structures and pore sizes in the range of 250-350 microns using a selective laser melting (SLM) system Renishaw AM400. Lack of fusion in additive manufacturing results in partially sintered metal particles on both interior and exterior surfaces of porous titanium scaffolds, which necessitates the investigation of seeking an effective polishing method for removing the partially melted particles on the surface of an intricate designed porous implant to achieve a better surface morphology and roughness that augments osseointegration. In this paper, three polishing methods were examined. The experimental result shows that the electropolishing method is capable of effectively removing the incompletely fused particles but it is noteworthy that the parameters controlled during the experiment are crucial to preserve the lattice structure. Rotary abrasive flow polishing method is worth investigating in depth, if better control the direction and rate of flow, the better surface morphology and roughness can be achieved. Lastly, the ultrasonic polishing method was explored to investigate the dependence on the vibratory amplitude control.

Keywords: surface polishing, surface roughness, lattice structure, porous titanium scaffolds, metal additive manufacturing, osseointegration

1. Introduction

There are approximately 1 million cases of bone defects that require bone implants for patients every year in the United States [1], which demands bone regenerative technologies to provide more reliable and novel treatments. Conventional bone implants, particularly solid metal materials, have numerous limitations that do not provide sufficient treatment and rehabilitation, such as osseointegration and neovascularization for repairing the injuries of the bone [2, 3]. In contrast, a porous bone scaffold has a special interior structure through which bone cells, vessels, and capillaries can grow within and provides the insight to elicit neovascularization and integrate the growth of surrounding tissue, resulting in osseointegration in the scaffolds. Eventually, the interconnectivity between the implanted scaffolds and the host's bone will be strengthened [4]. Therefore, to take the advantage of Computer-aided design (CAD) and additive manufacturing technology, a customized porous metal implant can be introduced as an alternative treatment to bone implantation. 3D printing has been widely applied to different industrial and medical fields in recent years, this technology can furnish rapid manufacture of various designed parts in a short period of time compared with traditional manufacture, thus, by utilizing the CAD software, one

will be able to personalize the bone implants contingent upon the level of bone defects of the patient [5]. Nonetheless, unpolished porous titanium implants lack the desired level of osseointegration of bone cells due to poor surface finishing. Surface roughness is a substantial parameter that can affect the growth of bone cells and the anchorage between bones and implants which is identified as a hallmark of long-term successful implantation [6].

Bone consists of two portions-cancellous and cortical bones. Osteoblasts are responsible for the formation of a new bone matrix whereas osteoclasts reabsorb the mineralized bones, this is a cycling process and is known as bone remodeling [7]. Bone remodeling is essential for bone repair and regeneration, but there are several situations in which this self-sustaining process will halt. For instance, traumatic injuries with large areas of bone defects and necrosis around the damaged site will require external assistance like autograft, allograft, or implantation for functional regeneration [8]. Functional regenerative implantation must be capable of inducing a satisfactory level of osseointegration and gene expression of osteoblasts. In previous studies, it was shown that osteoblastic differentiation and some gene expressions performed optimally around the range of $1\mu\text{m}$ and $2\mu\text{m}$ (considered as medium-high roughness), but the optimal surface roughness for optimal performance of proliferation is smoother than the aforesaid range [9-11].

This proposed study will focus on a range of varying lattice structures scaffolds with unique unit cells (a mathematical concept that should not be confused with biological cells) that offer controllable pore size. Pore size and porosity are the primary concerns in the manufacturing of porous scaffolds because they impact the mechanical properties of an implant, such as elastic modulus and mechanical strength as well as the biological performance of the implant material [12]. Previous studies recommend that the ideal size of the pores within a titanium implant is in the range of $100\text{-}400\mu\text{m}$ [13, 14]. The lattice structure porous architecture is conceptualized in software using Computer-aided design (CAD) and the designed scaffolds in this study are in accordance so that it provides good mechanical functionality combined with mass transport to facilitate biological delivery and angiogenesis [15]. Due to the requirement for the scaffold structure to be porous enough for biocompatibility, it is imperative to make them with varying but continuous strut dimensions and shapes by defining a type of unit cell [15]. In this case, different lattice-structure designs of the basic cubic star (BC star), hexagons, vertex octagons, and prime cube will be investigated [16]. These unit cells will be replicated across the scaffold in a periodic manner using Rhinoceros and Grasshopper plugin [17]. Ideally, the scaffolds used in tissue engineering should be biocompatible, but they should also satisfy some structural and physical properties, such as the scaffold's permeability should be high enough to allow superior diffusion, facilitating nutrient intake and metabolic waste removal [18]. Within the scaffolds, the pores should be linked. Even if the scaffold porosity is large, material transport and cell migration would be hampered if the pores are not linked [19]. The surface area and pore size of the scaffolds should be appropriate [20]. A wide surface area allows for cell attachment and development, but a large pore volume is necessary to accept and then supply a sufficient cell mass for tissue healing. Porous materials' surface area/volume ratio is defined as the mean diameter of the pores. Researchers determined that ideal pore diameters for neovascularization were $5\mu\text{m}$, $5\text{-}15\mu\text{m}$ for fibroblast growth, $20\mu\text{m}$ for hepatocyte ingrowth, $100\text{-}350\mu\text{m}$ for bone regeneration, and about $500\mu\text{m}$ for fibrovascular tissues. The focus of our study is bone regeneration. Therefore, the target pore size for our scaffolds is in the range of $250\text{-}350\mu\text{m}$ [13, 14].

The scaffolds were printed by Selective Laser Melting (SLM), also known as Laser Powder Bed Fusion (LPBF), which is a cutting-edge manufacturing technology that is widely used for the fabrication of scaffolds as it provides the best freeform fabrication of complex geometries compared to other technologies along with a highly repeatable workflow [21]. The material choice is Ti-6Al-4V (90% titanium, 6% aluminum, 4% vanadium) owing to its high biocompatibility, young modulus, and corrosion resistance [22]. However, the process-associated high surface roughness makes it is of interest to develop suitable methods to eliminate the surface defects of partially sintered particles on the surface of complex geometry in the metal piece caused by lack of fusion.

There are numerous polishing methods that have been explored in previous research. For instance, the magnetic surface finishing is a process that uses a high-strength magnet mounted on a rotating shaft with a high RPM to generate a high-fluctuating magnetic field. The workpiece in this magnetic field along with granular magnetic abrasives made of both ferromagnetic materials such as iron and abrasive grains such as aluminum oxide or diamond powder is mostly mixed in a slurry and the finishing pressure on the workpiece created by the magnetic field [23]. Abrasive flow finishing polishes the metal parts with flowing abrasive slurry which strikes the surface of the metal and thus to remove the material [24]. Electropolishing smoothens the surface by removing some external materials employing electrical current and electrolyte [25], and ultrasonic polishing uses vibratory forces to remove the external surface material [26]. Yet, most of the polishing techniques merely apply to solid metal parts. Therefore, the main objective of this paper was challenging to remove partially sintered metal particles and reduce the surface roughness of four intricate structured scaffolds applying three polishing techniques: electropolishing, ultrasonic polishing, and the rotary abrasive flow polishing methods.

2. Materials and Methods

2.1 Design Process and Tools

The lattice to be designed can be defined in terms of a cellular structure, and cellular structured materials are generally described as being of two types of topologies that are stochastic or periodic [27]. Stochastic are randomized structures, whereas Periodic or non-stochastic are modeled after a unit cell. The focus of the case study is on periodic or non-stochastic lattice structures. The design process starts by creating a solid cylinder with a diameter of 5mm and height of 3mm in Rhinoceros CAD software [17]. The next step is to populate the scaffold with various unit cells using the crystallon library of the grasshopper plugin inside Rhinoceros. The process of creating the lattice structure is by converting the solid cylinder into a voxelized version of itself and then filling each voxel with a unit cell. Once the individual voxel vectors are available, the multipipe function was used to generate pipe meshes inside the voxels and use the bake function to generate a mesh object of our design.

Step 1 Voxelization: Grasshopper takes a Brep (our solid cylinder of radius 2.5 mm and height 3mm) and converts it into a voxelized form with side 1 in the X, Y, and Z directions using the Voxelization (Vd) function. **Step 2 Unit cell and lattice vectors:** The voxelized output is fed into a voxel populator function (CLF) which also requires a unit cell (CT) as a second input. The unit cells are selected from a drop-down menu called the unit cell selector. **Step 3 Multipipe and baking:** The output of step 2 is only vectors with the unit cells inside voxels. Feeding these vectors into a multipipe function (MP) which takes a node size (pipe radius) of 0.075 mm generates a pipe

diameter of 0.15 mm, and finally the “Bake” command was utilized to create a mesh of lattice structure.

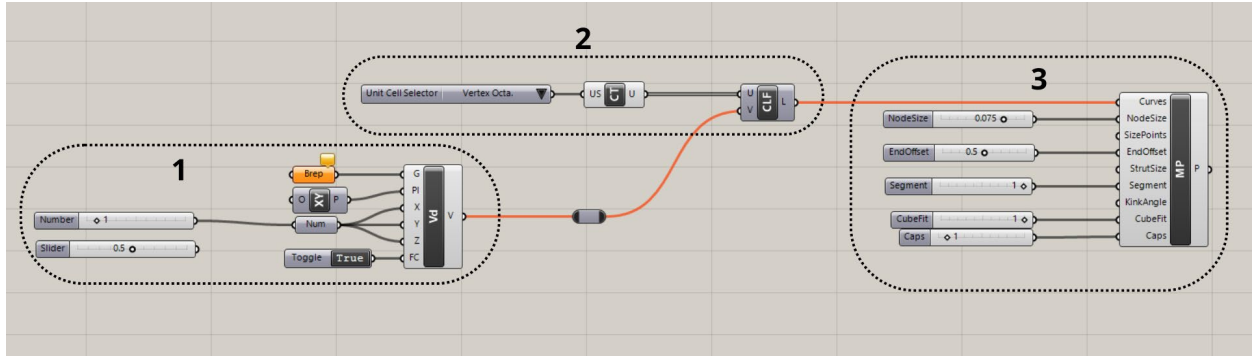


Figure 1. Grasshopper workboard with configuration for our study.

2.2 Designs of Lattice Structure

The crystalon library of the grasshopper plugin in Rhinoceros [15] provides a range of built-in unit cells that can be used to populate the scaffolds. The study was fine tuned to choose the following four designs:

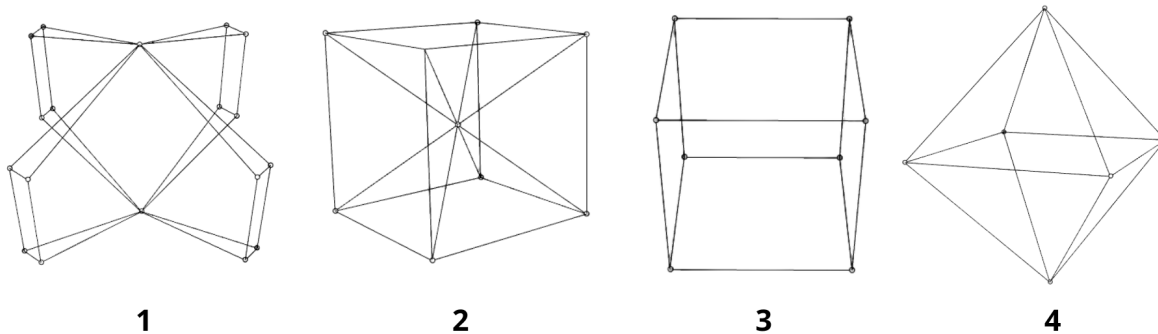


Figure 2. Unit cells: 1. Hexagon, 2. BC Star, 3. Prime cube, 4. Vertex Octagon

These particular unit cells shown in Figure 2 were designed to achieve the target pore size for the lattice structure is in the range of 300 microns [13, 14]. After multiple iterations of changing voxel cell size and variable pipe radius, it was determined that to get 300 micron pores a 0.075mm pipe diameter had to be used with the overall bounding box of each lattice being 1 unit per side during the voxelization (Step 1). The pore size was determined by measuring the smallest distance in each of the unit cells' geometries.

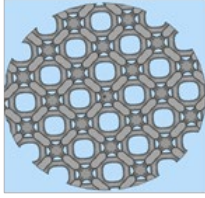
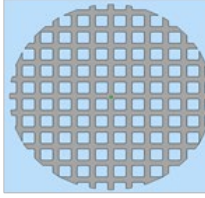
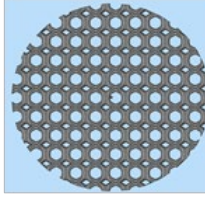
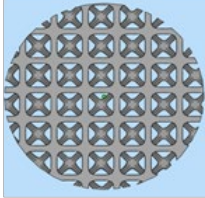
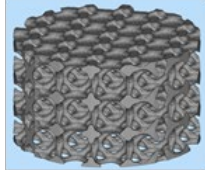
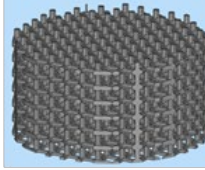
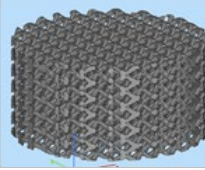
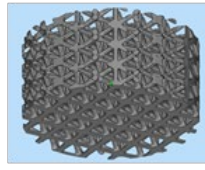




	Vertex Octagon	Prime Cube	Hexagon	BC Star
Top				
Perspective				
Actual				

Figure 3. Three Dimensional Models and Additively Manufactured Scaffolds of the Four Designs

2.3 Additively Manufacturing Porous Titanium Scaffolds

The SLM processing has been explained in detail by Wehmoller et al in a previous publication [28]. The SLM technology uses a laser beam of 70 microns in diameter to melt layers of Ti6Al4V in steps of 30 μ m along the z axis. The procedure consists of the following steps: The wiper blade first uses a tiny amount of metal powder to cover the metal base plate. The first layer is then microwelded to the base plate as a result of the laser beam sintering the powder at the laser's focus point in accordance with the scan pattern of the part. The plate is lowered by 0.03 mm after the first layer is sintered, and the recoated blade then spreads out a second coating of titanium powder on top of the first layer. The fresh powder layer is then merged onto the older layer once the laser beam hits the fresh powder. In this method, our implant gets fabricated in a layer-by-layer process, which is very much the same as stereolithography [29].

All the samples were made at a laser power of 200 W, with a beam diameter of approximately 70 μ m, an exposure time of 80 μ s, a point distance of 45 μ m, a hatch spacing of 105 μ m, along with a layer thickness of 30 μ m. The scanning was performed using a stripes scan pattern rotated by 67° for each new layer. The size of the Ti64 powder used in the study is 44 μ m in diameter and is classified as a 325-mesh powder.



Figure 4. Renishaw AM400 and Reduced Build Volume (RBV) unit

2.4 Surface Cleaning

Prior to further experiments, ultrasonic cleaning was applied to remove unmelted titanium residues on the surface of the scaffolds. First, immerse the scaffolds in the deionized water which is filtered by the Milli-Q water purification machine in a beaker, and put the beaker in a sonicator water bath and ultrasonically clean for 15 minutes at room temperature. Subsequently, ultrasonically clean the scaffolds that are soaked in the acetone with an aluminum foil covering the beaker for 35 minutes, and then clean them with deionized water for 15 minutes again. It is essential to repeat the aforementioned steps until there is no discoloration. Figure 5 shows the distinguishable appearance of the printed side and bottom side [30].









	Hexagon	Prime Cube	Vertex Octagon	BC Star
Printed Side				
Bottom Side				

Figure 5. Printed Side and Bottom Side of Cleaned Scaffolds

2.5 Surface Finishing

2.5.1 Rotary Abrasive Flow Polishing

This proposed rotary abrasive flow polishing method is inspired by magnetic assisted polishing, tumbling, and the abrasive flow polishing methods. The pore diameter of designed scaffolds is ranging from 300-400 microns. In an effort to polish the interior surface, micro-scale diamond powder (36-54 microns purchased from TechDiamondTool.com) was mixed with deionized water in a concentration of 2g/ml as the abrasive slurry. The experimental setup is exhibited in Figure 6, with which a 50mL beaker was placed on the magnetic stirrer, and a

cylindrical magnet was put into the beaker which can spin and interact to the magnetic field changes by the magnetic stirrer. Ultrasonically cleaned scaffolds were submerged by the abrasive slurry, and when the cylindrical magnet spins with magnetic stirrer, it creates a turbulent water vortex which drives the aqueous abrasive slurry to strike the surface of the scaffolds. The rotational speed was controlled within 800 to 1250 RPM, and the polishing process was done at room temperature for 10 hours.

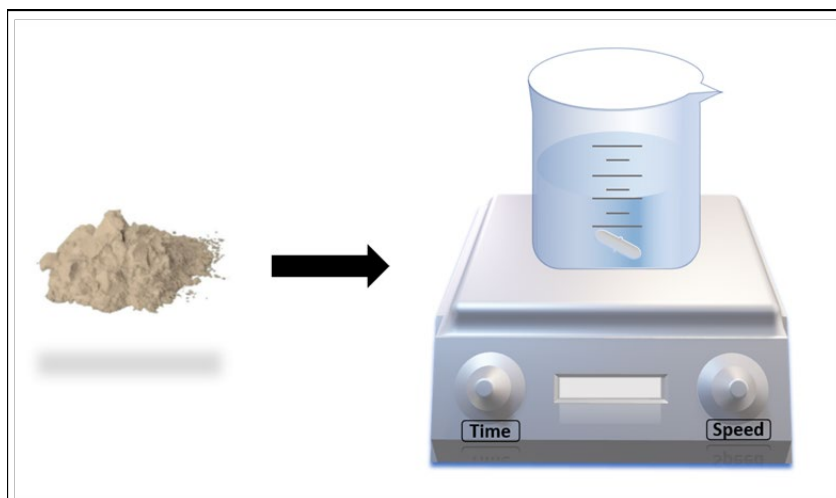


Figure 6. Experimental Setup of Rotary Abrasive Flow Polishing

2.5.2 Ultrasonic Polishing

Referring to previous research investigated by Wang et.al, we challenged ultrasonic polishing techniques in this paper. The ultrasonic model we utilized is Qsonica Sonicator, and the experimental setup is manifesting in Figure 7. A scaffold is fixed to the bottom surface of a 10mL beaker and sunked in the abrasive slurry of diamond powder with a concentration of 2g/mL. The 10mL beaker is sitting in a container filled with ice for temperature control. Afterwards, place the ultrasonic probe into the beaker without touching the bottom surface of it. Run the sonicator with 30% amplitude and 15-25 time pulse for 30 minutes [26].

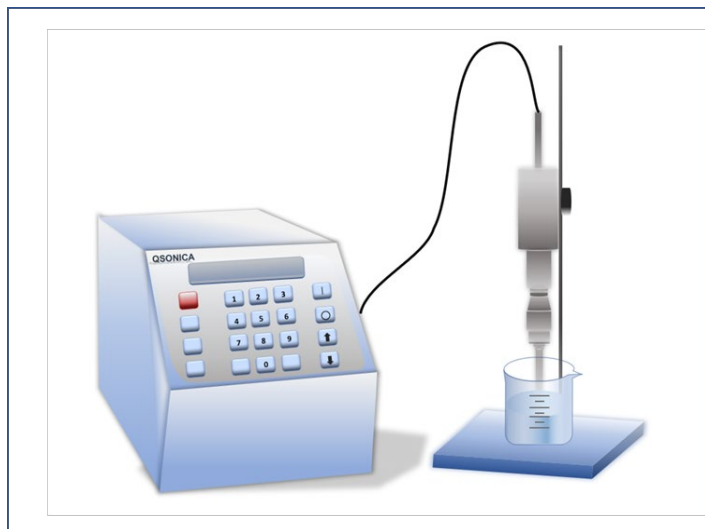


Figure 7. The Experimental Setup of Ultrasonic Polishing

2.5.3 Electropolishing

Four designed scaffolds were sent to Able Electropolishing Company for electropolishing which provides precise surface finishing. Alternate current (AC) input converts to direct current (DC) as an output, which connects to the cathode made of stainless-steel bar. The positive end, anode, connects to a rack that will be immersed in a bath of electrolyte which acts as conductor. When current flows through the system, the metal-contained chemical solution will react with cathode and thus remove the metal ions from the surface of the scaffolds. As a result, the total stock removal is 0.0005inches [31].

2.6 Characterization

2.6.1 Surface Morphology

The surface morphology of the polished titanium scaffolds is imaged using a scanning electron microscopy (SEM), Zeiss Supra 40VP Microscopy, after polished and ultrasonically cleaning shows in the Figure 9. One scaffold is adhered on a 3.2mm*8mm stub using double-sided carbon conductive tape. Eight SEM stubs were fixed in a SEM pin mount specimen holder, and then imaged at once. Two images were taken, one is 100 μ m scale and another one is 400 μ m scale for each scaffold.

2.6.2 Surface roughness measurement

A measurable area was chosen at random on the samples to measure the surface roughness using a white light Veeco interferometer. Each scaffold is infinite scanned and measured in half resolution, in 1 times scan speed, 50 times objective, 1 times FOV, 100 μ m backscan, 200 μ m length, and 3% modulation threshold. Unpolished surface challenged data losses, so we restored our data choosing 35 data restore pixels. The x-axis length is 126 μ m, which allows one to two cells to attach on.

2.6.3 Compression Test

The room temperature uniaxial compression tests were conducted at the Pacific Testing Laboratory, Inc. Each scaffold with sophisticated structure was tested separately using a united load frame (FM60R) and load cell (10K) with loading speed of 8.47 μ m/s to reveal the relationship between scaffold structures and strength.

2.6.4 Porosity Calculation

3. Results and Discussion

3.1 Surface Morphology of Scaffolds

The physical changes of unpolished and polished scaffolds are compared in Figure 8, the polishing process reduced the materials of scaffolds. In accordance with the SEM analysis, there are noticeable amounts of partially sintered particles on the unpolished surface, electropolished scaffolds are conspicuously smoother and most of the unsintered spherical particles were removed. Rotary abrasive flow polished group has obvious marks of abrasion on the surface that were caused by the friction and collision from diamond particles (Figure 9o), and has some material removal (Figure 9k) compared with the unpolished group. Ultrasonic group has a few marks of abrasion which are unnoticeably to observe.

Though the electropolished method shows the most significant morphological changes, the scaffolds were not able to maintain their structures due to the small size and the intricate interior

geometry during the electropolishing process, resulting in them breaking apart. As shown in Figure 8 and 9b, there was only a residual piece left after electropolished, this condition is consistently applied to three types of electropolished scaffolds- hexagon, prime cube, and BC star shown in Figure 9f, j, n, r, v, z, and D. Interestingly, the main skeleton of the vertex octagon was preserved.

















	Hexagon	Prime Cube	Vertex Octagon	BC Star
Unpolished				
Electropolished				
Rotary Abrasive Polished				
Ultrasonic Polished				

Figure 8. Comparison of physical appearance changes by three polishing methods

3.2 Surface Roughness

A measurable area was chosen at random on the samples to measure the surface roughness using a white light Veeco interferometer. Three unpolished designs are laborious to measure due to the irregular structure of the printed surface and we were unable to find a measurable area on an unpolished BC star. The equipment used is sensitive to the changes of height, and referring to the SEM images in Figure 9, the designs of scaffolds have intricate lattice structure and have no flat surface. Both aforesaid reasons caused large areas of data losses during the measuring process, black spaces in the Figure 10 indicate data losses.

After patching some hypothetical data to the measurement of unpolished scaffolds by supplementing some pixels, unpolished hexagon shows a Ra of $5.37\mu\text{m}$, unpolished prime cube shows a Ra of $3.35\mu\text{m}$, and the vertex octagon shows a Ra of $2.47\mu\text{m}$. Rotary abrasive flow polished scaffolds are found much easier to measure than the polished one, in proportion to rotary abrasive flow polishing group of Figure 9, the printed surfaces were abraded and seemed more flat than the unpolished surface. Consequently, the result of polished ones is more accurate and reliable than the unpolished one's, and it is observable when examining the unpolished and polished 3D results in Figure 9. The Ra for polished hexagon is $4.51\mu\text{m}$, for polished prime cube, the Ra is $4.00\mu\text{m}$, and the Ra for the polished vertex octagon is $0.76\mu\text{m}$.

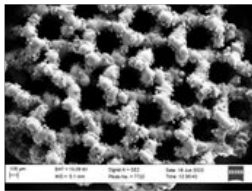
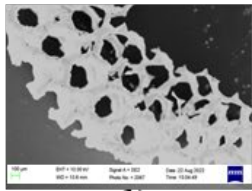
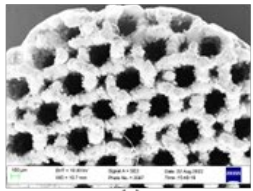
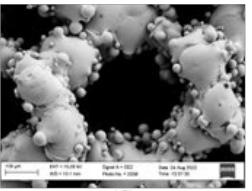
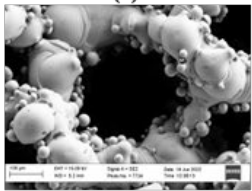
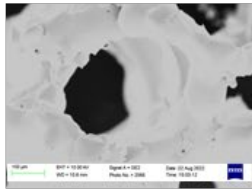
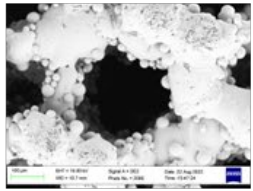
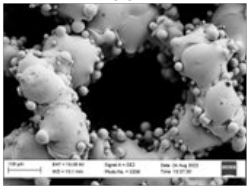
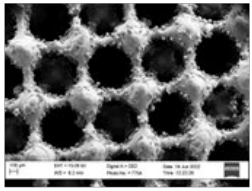
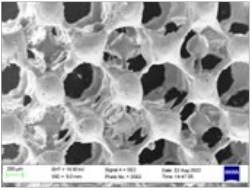
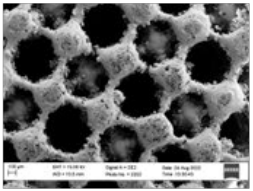
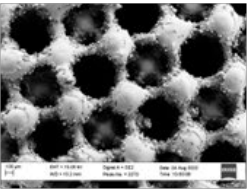
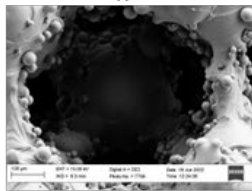
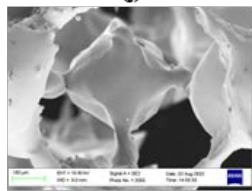
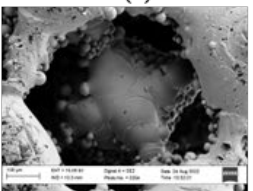
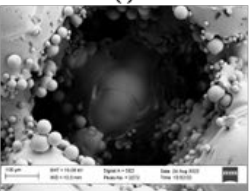
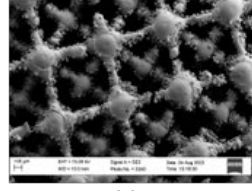
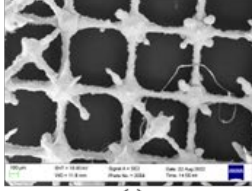

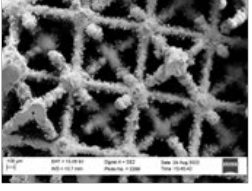
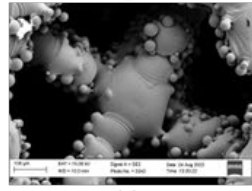
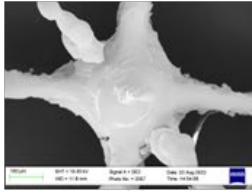
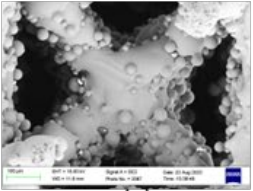
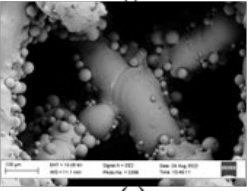
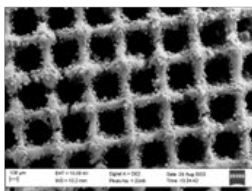
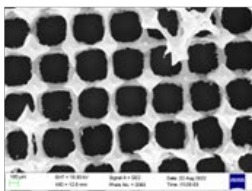
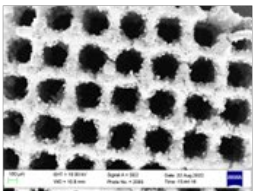
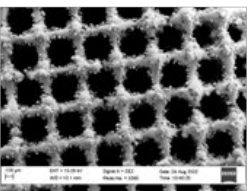
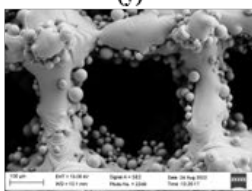
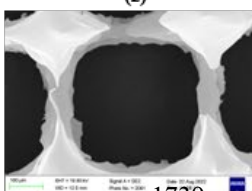
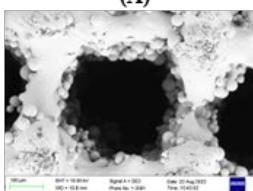
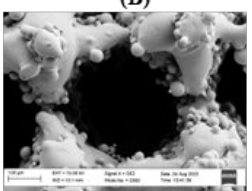
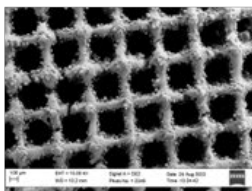
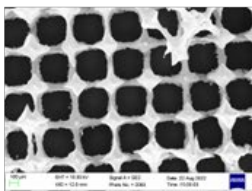
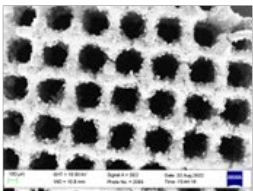
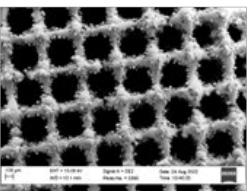
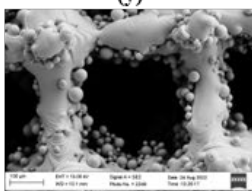
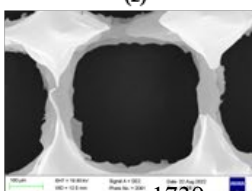
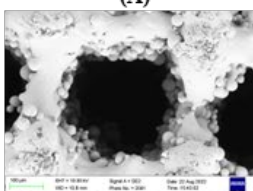
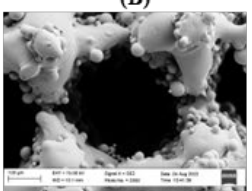
	Unpolished	Electropolished	Rotary Abrasive Polished	Ultrasonically Polished
Hexagon	 (a)	 (b)	 (c)	 (d)
	 (e)	 (f)	 (g)	 (h)
	 (i)	 (j)	 (k)	 (l)
	 (m)	 (n)	 (o)	 (p)
BC Star	 (q)	 (r)	 (s)	 (t)
	 (u)	 (v)	 (w)	 (x)
	 (y)	 (z)	 (A)	 (B)
	 (C)	 (D)	 (E)	 (F)
Prime Cube	 (y)	 (z)	 (A)	 (B)
	 (C)	 (D)	 (E)	 (F)

Figure 9. SEM images of four designed scaffolds before and after polished by three polishing methods: (a,e) unpolished hexagon, (b,f) electropolished hexagon, (c,g) rotary abrasive flow polished hexagon, (d,h) ultrasonically polished hexagon, (i,m) unpolished vertex octagon , (j,n) electropolished vertex octagon, (k,o) rotary abrasive flow polished vertex octagon, (l,p) ultrasonically polished vertex octagon , (q,u) unpolished BC star, (r,v) electropolished BC star, (s,w) rotary abrasive flow polished BC star, (t,x) ultrasonically polished BC star, (y,C) unpolished prime cube, (z,D) electropolished prime cube, (A,E) rotary abrasive flow polished prime cube, (B,F) ultrasonically polished prime cube

	Unpolished	Rotary Abrasive Flow Polished
Hexagon	<p>(a)</p> <p>(c)</p>	<p>(b)</p> <p>(d)</p>
Prime Cube	<p>(e)</p> <p>(g)</p>	<p>(f)</p> <p>(h)</p>
Vertex Octagon	<p>(i)</p> <p>(k)</p>	<p>(j)</p> <p>(l)</p>

Figure 10. Surface roughness measured by Veeco: (a) 2D result of unpolished hexagon, (b) 2D result of a rotary abrasive flow polished hexagon, (c) 3D result of unpolished hexagon, (d) 3D result of a rotary abrasive flow polished hexagon, (e) 2D result of unpolished prime cube, (f) 2D result of a rotary abrasive flow polished prime cube, (g) 3D result of a unpolished prime cube, (h) 3D result of a rotary abrasive flow polished prime cube, (i) 2D result of unpolished vertex octagon, (j) 2D result of a rotary abrasive flow polished vertex octagon, (k) 3D result of a unpolished vertex octagon, (l) 3D result of a rotary abrasive flow polished vertex octagon

3.3 Compression Test

Table 1 shows the maximum load and compressive strength of scaffolds with various structures. Figure 11 compares the strength-strain curves of the samples. The compressive strength of four scaffolds shows that it is of interest to cover optimization of such structures in the future works which can fulfill the strength requirements in bone implant applications. Since samples have been failed earlier than the maximum load was utilized and only the first maximum load was used for strength calculations. Hexagon yields the highest load of 645 N and the lowest load was observed in Vertex octagon and BC star structures at 235.8 and 244.7 N respectively. The actual cross section area of scaffolds were measured and highest compressive strength was observed in prime cube scaffold at 107.8 MPa, Vertex octagon scaffold yields the lowest compressive strength at 16.7 MPa.

Table 1. Maximum load and compressive strength

Specimen (scaffold)	Maximum load (N)	Compressive strength (MPa)
Prime Cube	462.6	107.8
Vertex Octagon	235.8	16.7
BC Star	244.7	23.8
Hexagon	645	41.6

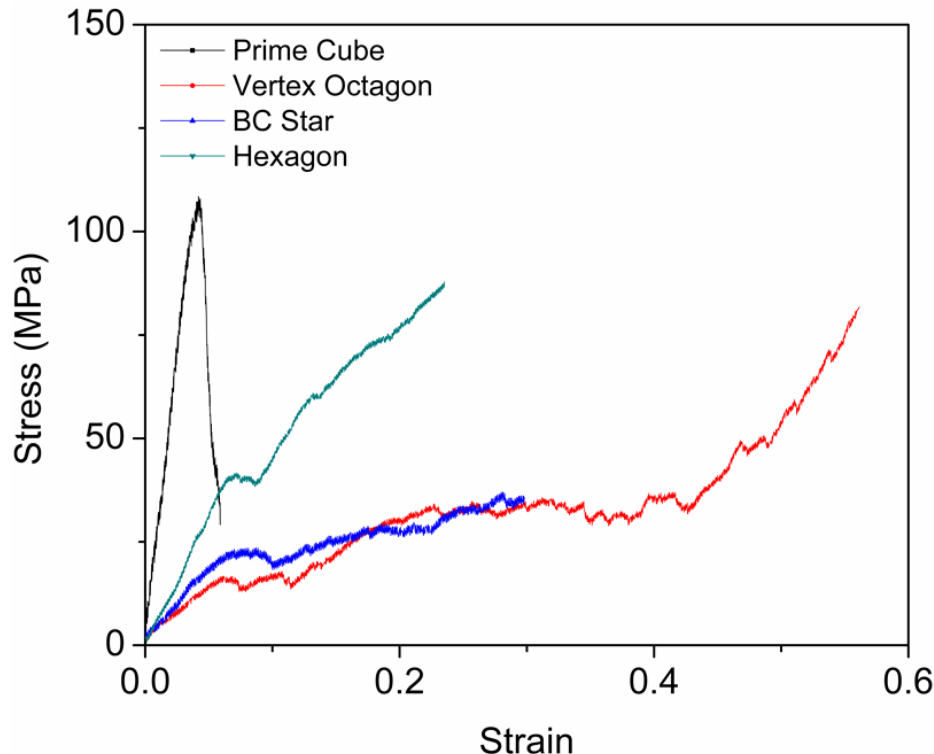


Figure 11. Stress-strain curves of four scaffolds

4. Conclusion

In this study, three surface polishing methods were investigated preliminarily for the bone implant scaffolds, and the main conclusions are listed below:

1. Electropolishing is capable of smoothing intricate lattice structures, while the optimized experimental parameters are desired to accommodate the size and the complexity of the scaffolds. Rotary abrasive flow polishing is effective to some extent, but to refine the effectiveness of the method, the direction and rate of the flow must be controlled in favor of augmenting the interior surface polish. Amplitude might be adjusted to improve the vibratory strength for ultrasonic polishing.
2. From the result of surface roughness and surface morphology of rotary abrasive flow polished scaffolds, the vertex octagon shows the smoothest polished surface roughness and largest amount of material removal besides electropolished ones.
3. Prime cube scaffold possesses the highest compressive strength when compared to the other three scaffolds. Strength of 107.8 MPa was found in prime cube and Vertex Octagon yields the lowest strength of 16.7 MPa, it shows that structure plays an important role in strength of scaffold and optimization of such structure is of interest to be conducted in the future works.

Acknowledgments

This research was supported by the U.S. NASA MUREP Institutional Research Opportunity (MIRO) program (80NSSC19M0200), NASA MUREP High Volume (80NSSC22M0132), and partially carried out at the Jet Propulsion Laboratory, California Institute of Technology, under a contract with the National Aeronautics and Space Administration (80NM0018D0004).

References

1. Holtorf, H.L., J.A. Jansen, and A.G. Mikos. *Modulation of Cell Differentiation in Bone Tissue Engineering Constructs Cultured in a Bioreactor*. in *Tissue Engineering*. 2007. Boston, MA: Springer US.
2. Pałka, K. and R. Pokrowiecki, *Porous Titanium Implants: A Review*. *Advanced Engineering Materials*, 2018. **20**(5): p. 1700648.
3. Salgado, A.J., O.P. Coutinho, and R.L. Reis, *Bone tissue engineering: state of the art and future trends*. *Macromol Biosci*, 2004. **4**(8): p. 743-65.
4. Dabrowski, B., et al., *Highly porous titanium scaffolds for orthopaedic applications*. *J Biomed Mater Res B Appl Biomater*, 2010. **95**(1): p. 53-61.
5. Wang, C., et al., *3D printing of bone tissue engineering scaffolds*. *Bioactive Materials*, 2020. **5**(1): p. 82-91.
6. Raina, D.B., et al., *Biomodulation of an implant for enhanced bone-implant anchorage*. *Acta Biomaterialia*, 2019. **96**: p. 619-630.
7. Hadjidakis, D.J. and Androulakis, II, *Bone remodeling*. *Ann N Y Acad Sci*, 2006. **1092**: p. 385-96.
8. Bose, S., S. Vahabzadeh, and A. Bandyopadhyay, *Bone tissue engineering using 3D printing*. *Materials Today*, 2013. **16**(12): p. 496-504.
9. Andrukhov, O., et al., *Proliferation, behavior, and differentiation of osteoblasts on surfaces of different microroughness*. *Dental Materials*, 2016. **32**(11): p. 1374-1384.
10. Wennerberg, A. and T. Albrektsson, *Effects of titanium surface topography on bone integration: a systematic review*. *Clin Oral Implants Res*, 2009. **20 Suppl 4**: p. 172-84.
11. Albrektsson, T. and A. Wennerberg, *Oral implant surfaces: Part 1--review focusing on topographic and chemical properties of different surfaces and in vivo responses to them*. *Int J Prosthodont*, 2004. **17**(5): p. 536-43.
12. Mediaswanti, K., et al., *Biomimetic Creation of Surfaces on Porous Titanium for Biomedical Applications*. *Advanced Materials Research*, 2014. **896**: p. 259-262.
13. Klawitter, J.J. and S.F. Hulbert, *Application of porous ceramics for the attachment of load bearing internal orthopedic applications*. *Journal of Biomedical Materials Research*, 1971. **5**(6): p. 161-229.
14. Whang, K., et al., *Engineering Bone Regeneration with Bioabsorbable Scaffolds with Novel Microarchitecture*. *Tissue Engineering*, 1999. **5**(1): p. 35-51.
15. Hollister, S.J., *Porous scaffold design for tissue engineering*. *Nature Materials*, 2005. **4**(7): p. 518-524.
16. Yan, C., et al., *Evaluation of light-weight AlSi10Mg periodic cellular lattice structures fabricated via direct metal laser sintering*. *Journal of Materials Processing Technology*, 2014. **214**: p. 856–864.
17. McNeel, R. *Rhinoceros 3D, Version 6.0*. Associates, Seattle, WA 2010 [cited 2022 June 22].
18. Karande, T.S., J.L. Ong, and C.M. Agrawal, *Diffusion in musculoskeletal tissue engineering scaffolds: design issues related to porosity, permeability, architecture, and nutrient mixing*. *Ann Biomed Eng*, 2004. **32**(12): p. 1728-43.
19. Mooney, D.J., et al., *Novel approach to fabricate porous sponges of poly(d,l-lactic-co-glycolic acid) without the use of organic solvents*. *Biomaterials*, 1996. **17**(14): p. 1417-1422.

20. Rajagopalan, S. and R.A. Robb, *Schwarz meets Schwann: design and fabrication of biomorphic and durataxic tissue engineering scaffolds*. *Med Image Anal*, 2006. **10**(5): p. 693-712.
21. Hollister, S.J., *Scaffold design and manufacturing: from concept to clinic*. *Adv Mater*, 2009. **21**(32-33): p. 3330-42.
22. Zuo, W., et al., *Properties improvement of titanium alloys scaffolds in bone tissue engineering: a literature review*. *Annals of translational medicine*, 2021. **9**(15): p. 1259-1259.
23. Yamaguchi, H., O. Fergani, and P.Y. Wu, *Modification using magnetic field-assisted finishing of the surface roughness and residual stress of additively manufactured components*. *Cirp Annals-manufacturing Technology*, 2017. **66**: p. 305-308.
24. Bhattacharyya, B. and B. Doloi, *Chapter Eight - Advanced finishing processes*, in *Modern Machining Technology*, B. Bhattacharyya and B. Doloi, Editors. 2020, Academic Press. p. 675-743.
25. Yang, L. (n.d.). Use of electropolishing for uniform surface treatment of metal components with complex external geometries.
26. Wang, J., J. Zhu, and P.J. Liew, *Material Removal in Ultrasonic Abrasive Polishing of Additive Manufactured Components*. *Applied Sciences*, 2019. **9**(24).
27. Rajesh S. Kumar, David L. McDowell, Multifunctional design of two-dimensional cellular materials with tailored mesostructure, *International Journal of Solids and Structures*, Volume 46, Issues 14–15, 2009, Pages 2871-2885
28. M. Wehmöller, P.H. Warnke, C. Zilian, H. Eufinger, Implant design and production—a new approach by selective laser melting, *International Congress Series*, Volume 1281, 2005, Pages 690-695,
29. Ferry P.W. Melchels, Jan Feijen, Dirk W. Grijpma, A review on stereolithography and its applications in biomedical engineering, *Biomaterials*, Volume 31, Issue 24, 2010, Pages 6121-6130
30. Li B, Hesar BD, Zhao Y, Ding L. Design and additive manufacturing of porous titanium scaffolds for optimum cell viability in bone tissue engineering. *Proceedings of the Institution of Mechanical Engineers, Part B: Journal of Engineering Manufacture*. July 2020. doi:10.1177/0954405420937565
31. *Electropolishing service for Stainless Steel & other metal parts: Able*. Able Electropolishing. (2021, February 12). Retrieved August 26, 2022, from <https://www.ableelectropolishing.com/services/electropolishing/>